The Astrophysical Journal, 923:56 (12pp), 2021 December 10 https://doi.org/10.3847/1538-4357/ac2cbf

A Comparison of Circumgalactic Mg II Absorption between the TNG50 Simulation and the MEGAFLOW Survey

Daniel DeFelippis[1], Nicolas F. Bouché[2], Shy Genel[3,4], Greg L. Bryan[1,3], Dylan Nelson[5], Federico Marinacci[6], and Lars Hernquist[7]

[1] Department of Astronomy, Columbia University, 550 West 120th Street, New York, NY 10027, USA; d.defelippis@columbia.edu
[2] Univ Lyon, Univ Lyon1, Ens de Lyon, CNRS, Centre de Recherche Astrophysique de Lyon UMR5574, F-69230 Saint-Genis-Laval, France
[3] Center for Computational Astrophysics, Flatiron Institute, 162 Fifth Avenue, New York, NY 10010, USA
[4] Columbia Astrophysics Laboratory, Columbia University, 550 West 120th Street, New York, NY 10027, USA
[5] Universität Heidelberg, Zentrum für Astronomie, Institut für theoretische Astrophysik, Albert-Ueberle-Str. 2, D-69120 Heidelberg, Germany
[6] Department of Physics and Astronomy "Augusto Righi," University of Bologna, Via Gobetti 93/2, I-40129 Bologna, Italy
[7] Harvard-Smithsonian Center for Astrophysics, 60 Garden Street, Cambridge, MA 02138, USA
Received 2021 February 16; revised 2021 September 17; accepted 2021 October 3; published 2021 December 10

Abstract

The circumgalactic medium (CGM) contains information on gas flows around galaxies, such as accretion and supernova-driven winds, which are difficult to constrain from observations alone. Here, we use the high-resolution TNG50 cosmological magnetohydrodynamical simulation to study the properties and kinematics of the CGM around star-forming galaxies in $10^{11.5}$–$10^{12}\,M_{\odot}$ halos at $z \simeq 1$ using mock Mg II absorption lines, which we generate by postprocessing halos to account for photoionization in the presence of a UV background. We find that the Mg II gas is a very good tracer of the cold CGM, which is accreting inward at inflow velocities of up to $50\,\mathrm{km\,s^{-1}}$. For sight lines aligned with the galaxy's major axis, we find that Mg II absorption lines are kinematically shifted due to the cold CGM's significant corotation at speeds up to 50% of the virial velocity for impact parameters up to 60 kpc. We compare mock Mg II spectra to observations from the MusE GAs FLow and Wind (MEGAFLOW) survey of strong Mg II absorbers ($\mathrm{EW}_0^{2796\,\text{Å}} > 0.5$ Å). After matching the equivalent-width (EW) selection, we find that the mock Mg II spectra reflect the diversity of observed kinematics and EWs from MEGAFLOW, even though the sight lines probe a very small fraction of the CGM. Mg II absorption in higher-mass halos is stronger and broader than in lower-mass halos but has qualitatively similar kinematics. The median-specific angular momentum of the Mg II CGM gas in TNG50 is very similar to that of the entire CGM and only differs from non-CGM components of the halo by normalization factors of $\lesssim$1 dex.

Unified Astronomy Thesaurus concepts: Galaxy formation (595); Galaxy dynamics (591); Galaxy kinematics (602); Galaxy structure (622); Circumgalactic medium (1879); Hydrodynamical simulations (767)

1. Introduction

The accretion of gas onto disk galaxies is a fundamental part of galaxy formation and evolution, as gas within disks is continually used to form stars and must therefore be regularly replenished (e.g., Putman 2017). All such gas, whether pristine gas from cosmological inflows or recycled gas in the process of reaccreting, must pass through the local environment surrounding galaxies, often called the circumgalactic medium (CGM). The CGM might contain a substantial amount of angular momentum as shown by many studies of galaxy simulations (e.g., Stewart et al. 2011; Danovich et al. 2015; DeFelippis et al. 2020). As the gas accretes onto the galaxy, the angular momentum will flow inward too, meaning the CGM is a source not just of the mass of the disk, but its angular momentum as well.

Not all gas surrounding galaxies is inflowing though: the CGM also contains outflowing gas ejected from the galaxy by feedback from supernovae and active galactic nuclei (AGN), which is capable of affecting the way in which CGM gas eventually joins the galaxy (DeFelippis et al. 2017). All of these physical processes occur concurrently and result in a multiphase environment shown in observations to have complex kinematics (see Tumlinson et al. 2017, and references therein).

A large number of recent observations of the CGM have been accomplished through absorption line studies of background quasars through dedicated surveys (e.g., Liang & Chen 2014; Borthakur et al. 2015; Kacprzak et al. 2015). For instance, some surveys are constructed by cross-correlating quasar absorption lines with spectroscopic redshift surveys such as the Keck Baryonic Structure Survey (KBSS; Rakic et al. 2012; Rudie et al. 2012; Turner et al. 2014) or with photometric surveys like the Sloan Digital Sky Survey (SDSS; Huang et al. 2016; Lan & Mo 2018; Lan 2020). Other CGM surveys attempt to either match individual absorption lines to known galaxies (i.e., are "galaxy selected"), like the COS-Halos (e.g., Tumlinson et al. 2011; Werk et al. 2013; Borthakur et al. 2016; Burchett et al. 2019), COS-LRG (Chen et al. 2018; Zahedy et al. 2019), and the low-redshift Keck surveys conducted at Keck Observatory (Ho et al. 2017; Martin et al. 2019), or match galaxies near known absorbers (i.e., "absorber selected") such as the MusE GAs FLOw and Wind survey (MEGAFLOW; Schroetter et al. 2016, 2019, 2021; Wendt et al. 2021; Zabl et al. 2019, 2020, 2021). In these surveys, there is generally only one quasar sight line per galaxy, but in certain rare cases it is possible to find multiple sight lines associated with a single galaxy through multiple quasars (Bowen et al. 2016), a single multiply lensed quasar (Chen et al. 2014; Zahedy et al. 2016; Kulkarni et al. 2019), an extended lensed quasar (Lopez et al. 2018), or even an extended background galaxy (Diamond-Stanic et al. 2016).

The Mg II ion has been a focus of many recent surveys including the Mg II Absorber-Galaxy Catalog (MAGIICAT; Chen & Tinker 2008; Chen et al. 2010a; Nielsen et al. 2013a, 2013b, 2015), the Magellan MagE Mg II (M3) Halo Project (Chen et al. 2010a, 2010b; Huang et al. 2021), the MUSE Analysis of Gas around Galaxies Survey (MAGG; Dutta et al. 2020), the PRIsm MUlti-object Survey (PRIMUS; Coil et al. 2011; Rubin et al. 2018), and the aforementioned MEGAFLOW survey, as well as individual absorbers (e.g., Lopez et al. 2020). These studies belong to a long history of Mg II λ2796 absorption line surveys (e.g., Bergeron & Boissé 1991; Bergeron et al. 1992; Steidel & Sargent 1992), which unveiled the first galaxy–absorber pairs at intermediate redshifts. Though not the focus of this paper, Mg II has also been seen in emission in extended structures around the galaxy and in the CGM (e.g., Rubin et al. 2011; Rickards Vaught et al. 2019; Rupke et al. 2019; Burchett et al. 2021; Zabl et al. 2021).

Along with this wealth of Mg II observations, researchers in recent years have found Mg II kinematics to be correlated over large spatial scales. In particular, both Bordoloi et al. (2011) and Bouché et al. (2012) found a strong dependence of Mg II absorption on azimuthal angle: specifically, more absorption near $\phi = 0°$ and 90° and a lack of absorption near 45°. This type of absorption distribution is generally interpreted as bipolar outflows along the minor axis and inflows along the major axis. In this context, both galaxy-selected (e.g., Ho et al. 2017; Martin et al. 2019) and absorption-selected Mg II studies (e.g., Kacprzak et al. 2012; Bouché et al. 2013, 2016; Zabl et al. 2019) have given support to the interpretation of accretion of gas from the CGM onto the galaxy. These Mg II studies show that when sight lines are located near the major axis of the galaxy there are clear signatures of corotating cold gas with respect to the galaxy kinematics.

However, despite such extensive observational data, developing a general understanding of cold gas in the CGM from the Mg II line alone remains difficult due to the limited spatial information provided by the observational technique (though IFU mapping of lensed arcs in e.g., Lopez et al. 2020, Mortensen et al. 2021, and Tejos et al. 2021 can improve this in the future), as well as the fact that Mg II gas may not be representative of the entire cold phase of the CGM. To study more physically fundamental properties of the CGM, it is therefore necessary to turn to galaxy simulations.

In cosmological simulations (see Vogelsberger et al. 2020 for a review), the CGM has been notoriously difficult to model accurately due to the need to resolve very small structures (e.g., Hummels et al. 2019; Peeples et al. 2019; Suresh et al. 2019; Corlies et al. 2020). Nonetheless, the CGM has been shown to preferentially align with and rotate in the same direction of the galaxy, especially near the galaxy's major axis (Stewart et al. 2013, 2017; Ho et al. 2019; DeFelippis et al. 2020), which is qualitatively consistent with observations in the same spatial region of the CGM (e.g., Zabl et al. 2019). However, this general qualitative agreement between simulations and observations is difficult to put on firm ground quantitatively due to the inherent differences between observations and simulations.

In this paper, we analyze a set of halos from the TNG50 simulation (Nelson et al. 2019; Pillepich et al. 2019) using the Trident tool (Hummels et al. 2017) to model the ionization state of the CGM and then perform a quantitative comparison of the kinematics of the cool ($T \lesssim 3 \times 10^4$ K) CGM traced by Mg II absorption to major-axis sight lines from the MEGAFLOW survey (Zabl et al. 2019) while attempting to match the observational selection criteria as described in Section 2. We note that our comparison to MEGAFLOW galaxies with stellar masses $M_* \sim 10^{10}\,M_\odot$ is complementary to that of both Nelson et al. (2020), who study the origins of cold CGM gas of very massive galaxies ($M_* > 10^{11}\,M_\odot$), and Nelson et al. (2021), who study properties of extended Mg II emission in the CGM.

The paper is organized as follows. In Section 2, we describe the TNG50 simulation and MEGAFLOW sample used in the comparison, and we outline the analysis pipeline used to generate mock observations. In Section 3, we describe our main results, first by comparing the simulated and real observations, then by analyzing the features of the simulation that give rise to the properties of the mock observations. In Section 4, we discuss the implications of our results for the role of the CGM in galaxy formation, and we summarize our findings in Section 5.

2. Methods

2.1. Simulations

We utilize the TNG50 simulation (Nelson et al. 2019; Pillepich et al. 2019), the highest-resolution version of the IllustrisTNG simulation suite (Marinacci et al. 2018; Naiman et al. 2018; Nelson et al. 2018; Pillepich et al. 2018; Springel et al. 2018), which is itself based on the original Illustris simulation (Vogelsberger et al. 2014a, 2014b). TNG50 evolves a periodic $\approx(52\,\mathrm{Mpc})^3$ box from cosmological initial conditions to $z = 0$ with the moving-mesh code Arepo (Springel 2010; Weinberger et al. 2020). It has a baryonic mass resolution of $\sim 8.5 \times 10^4\,M_\odot$ per cell, which is a factor of $\approx$16 better than the resolution of TNG100. We discuss the effect of simulation resolution on our results later in Section 3.

2.2. Observational Data

The MEGAFLOW survey (N. Bouché et al. 2021, in preparation) consists of a sample of 79 Mg II $\lambda\lambda$2796, 2803 absorbers in 22 quasar lines of sight observed with the Multi-Unit Spectroscopic Explorer (MUSE; Bacon et al. 2006). The quasars were selected to have at least three Mg II absorbers from the Zhu & Ménard (2013) SDSS catalog in the redshift range $0.4 < z < 1.4$ such that the [O II] $\lambda\lambda$3727,3729 galaxy emission lines fell within the MUSE wavelength range (4800–9300 Å). A threshold on the rest-frame equivalent width of ∼0.5–0.8 Å was also imposed on each absorber.

For this paper, we focus on a preliminary subset of the MEGAFLOW sample of Mg II absorber–galaxy pairs whose quasar location is positioned within 35° of the major axis of the host galaxy (Zabl et al. 2019). This subset consists of nine absorber–galaxy pairs with redshifts $0.5 < z < 1.4$ and impact parameters (b) ranging from 13 to 65 kpc with a mean of ≈34 kpc. Zabl et al. (2019) found that the Mg II gas in these absorbers show a strong preference for corotation with their corresponding host galaxies.

The galaxies in Zabl et al. (2019) are both fairly isolated by having at most one companion within 100 kpc, and star forming with [O II] fluxes $f_{\mathrm{OII}} > 4 \times 10^{-17}\,\mathrm{erg\,s^{-1}\,cm^{-2}}$, i.e., star formation rates $\gtrsim 1\,M_\odot\,\mathrm{yr}^{-1}$. The galaxies have stellar masses M_* ranging from $10^{9.3}$–$10^{10.5}\,M_\odot$ and halo masses M_{vir} ranging from $\approx 10^{11.4}$–$10^{12.2}\,M_\odot$, where M_{vir} is defined from the stellar mass–halo mass relation from Behroozi et al. (2010).

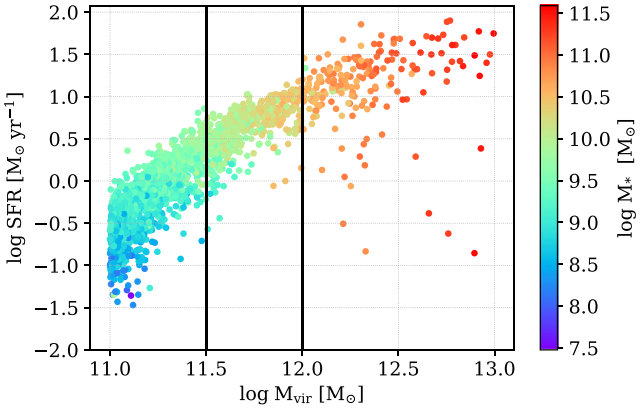

Figure 1. Star formation rate of the central galaxy vs. halo mass for all TNG50 halos between $10^{11}\,M_{\odot}$ and $10^{13}\,M_{\odot}$ at $z = 1$. Each point is colored by the stellar mass of the halo's central galaxy. Two thick vertical lines demarcate the halo mass range of the fiducial sample.

As Zabl et al. (2019) show, these halo masses generally match the Bryan & Norman (1998) definition of $M_{\rm vir}$.

2.3. Sample Selection and Forward Modeling

Figure 1 shows the central galaxies' instantaneous star formation rates (SFR) and stellar masses of all TNG50 halos in and around the mass range of interest. Since we aim to compare the Mg II absorption properties of mock line-of-sight (LOS) observations through TNG50 halos to those of major-axis sight lines of the MEGAFLOW survey, we first select a sample of simulated halos at $z = 1$ in the mass range $10^{11.5}\,M_{\odot} < M_{\rm halo} < 10^{12}\,M_{\odot}$ using the Bryan & Norman (1998) definition for $M_{\rm halo}$, which results in a sample of 495 halos. In the remainder of this paper, we will refer to this subsample as the "fiducial" sample. The chosen redshift is typical for the Zabl et al. (2019) sample, and the halo mass range covers the typical inferred virial masses of their halos. Nearly all of the halos in our fiducial sample host central galaxies with SFR $\gtrsim 1\,{\rm M}_{\odot}\,yr^{-1}$ and stellar masses of $\sim 10^{10}\,{\rm M}_{\odot}$, which is consistent with the MEGAFLOW subsample as described in Section 2.2.

For each halo, we adjust all velocities to be in the center-of-mass frame of the stars in the central galaxy, and we rotate it so that the stellar specific angular momentum of the central galaxy points in the $+z$-direction (the x- and y-directions are both arbitrary). With this geometry we then define a sight line in the x–z plane by the impact parameter b, the azimuthal angle α, and the inclination angle i, where b is the projected distance from the center of the galaxy in the y–z plane (i.e., "sky" plane), α is the angle above the rotational plane of the galaxy, and i is the angle of the sight line with respect to the sky plane. In this setup, edge-on and face-on views have $i = 90°$ and $i = 0°$, respectively (see Figure 1 of Zabl et al. 2019 for a sketch of the geometry described here). In order to mimic the observations of Zabl et al. (2019), we select sight lines through each halo at values of b ranging from 15 kpc to 60 kpc, $\alpha = 5°$ and 25°, and at $i = 60°$, representing the average inclination angle of a random sight line.

In order to generate observations of our TNG50 sample, we use the Trident package (Hummels et al. 2017), which calculates ionization parameters for outputs of galaxy simulations using properties of the simulated gas cells and Cloudy (Ferland et al. 2013) ionization tables. These tables take as input the gas temperature, density, metallicity, and cosmological redshift of each gas cell and provide ionization fractions and number densities of desired ions. We make use of the current development version of Trident[8] (v1.3), which itself depends on the current development version of yt[9] (v4.0). In this paper, we use a set of ion tables created assuming collisional ionization equilibrium, photoionization from a Faucher-Giguère et al. (2009) UV background, and self-shielding of neutral hydrogen (for details see Emerick et al. 2019 and Li et al. 2021), as this was the background radiation model used to evolve the TNG50 simulation. We also use the elemental abundance of magnesium in each gas cell tracked by the simulation rather than assuming a constant solar abundance pattern throughout the halo to achieve greater self-consistency with TNG50. We note, however, that our results are not particularly sensitive to either of these choices.

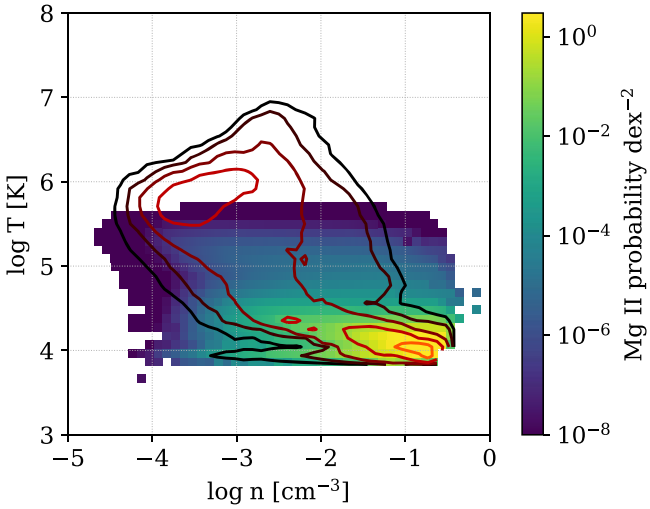

Figure 2. Temperature–number density phase diagram of a single TNG50 halo at $z = 1$, colored by the Mg II mass probability density per dex^2. Contours show the distribution of all gas mass in the halo.

Since our focus is on the Mg IIλ 2796 line, we show in Figure 2 a temperature–density phase diagram of the gas in one of the TNG50 halos from our sample, colored by the Mg II mass probability density. From this plot, it is clear that Mg II is mostly formed from the coldest ($\lesssim 10^{4.5}$ K) and densest ($\gtrsim 0.01\,{\rm cm}^{-3}$) gas in the halo, though some Mg II mass exists at a larger range of temperatures and densities. However, contours showing the total gas mass demonstrate that despite this large range in temperature and density, essentially none of the diffuse "hot" phase, comparable in mass to the cold phase, contributes to Mg II absorption. We also note here that for this analysis we are excluding star-forming gas as its temperature and density are defined using an effective equation of state (Springel & Hernquist 2003) and are therefore not analogous to the physical properties of non-star-forming gas. Properly modeling the physical properties of the star-forming gas (see Ramos Padilla et al. 2021 for an example of this technique) introduces a level of complexity not necessary for this analysis: we find that our results are not affected by the exclusion of this gas since our sight lines through the CGM rarely intersect any star-forming gas cells as most of them are within the galactic disk.

[8] http://trident-project.org
[9] https://yt-project.org

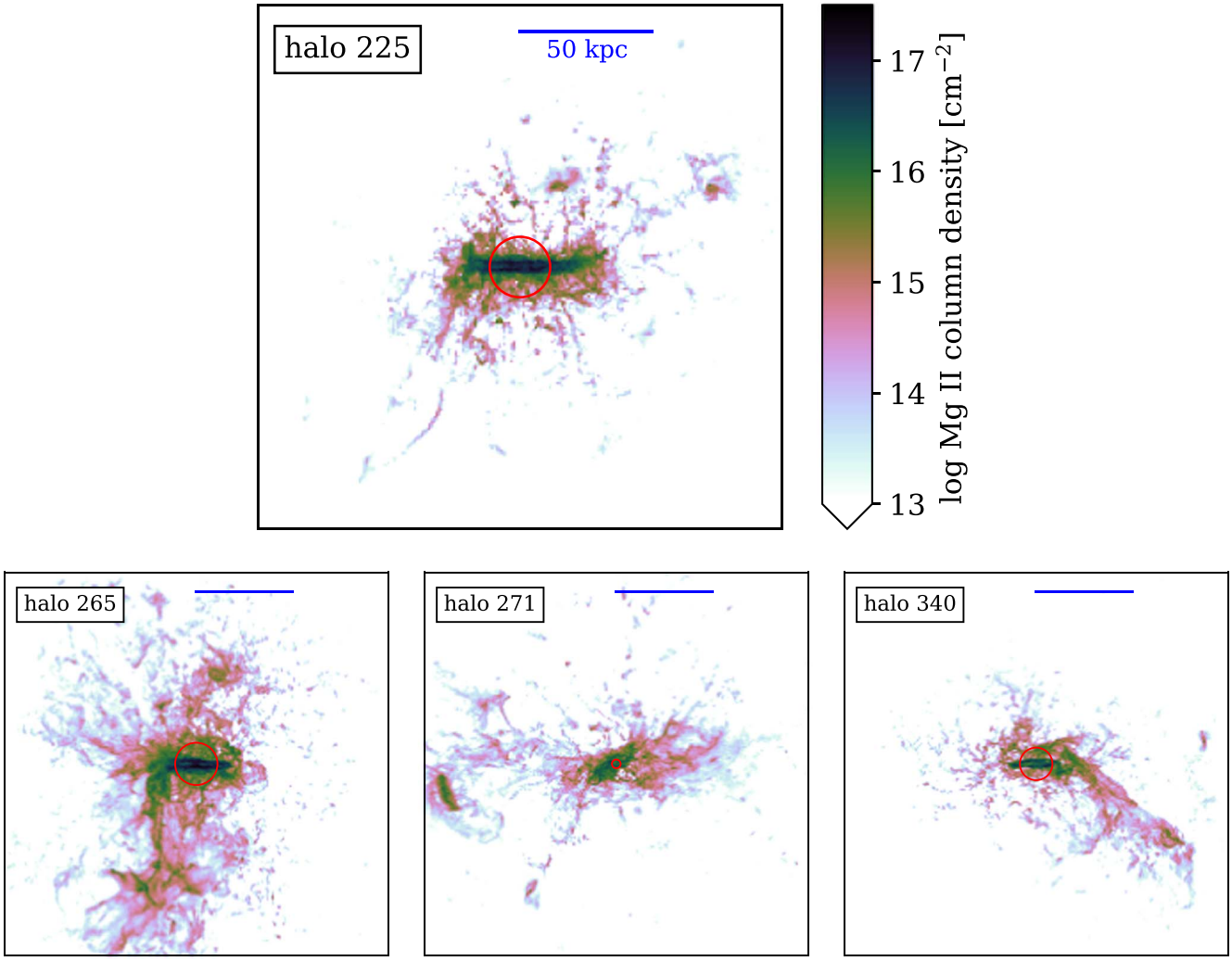

Figure 3. Mg II column density maps of four TNG50 halos from the fiducial halo mass bin of $10^{11.5}\,M_{\odot} < M_{\rm halo} < 10^{12}\,M_{\odot}$ at $z = 1$, aligned so the angular momentum vector of the stars in the central galaxy points along the vertical axis (i.e., edge-on). The lower limit of the color bar is chosen to approximate observational detection limits. The red circle in each panel is centered on the galaxy and has a radius of twice the galaxy's stellar half-mass–radius, and the blue scale-bar shows a distance of 50 kpc on the maps. The complexity and diversity of Mg II structure in the CGM of similar-mass halos are evident even in this small sample.

3. Results

We first present in Section 3.1 the results of directly comparing the Mg II properties of TNG50 and MEGAFLOW using the analysis described in Section 2. Then, we further analyze the 3D kinematic properties of the Mg II-bearing gas from TNG50 in Section 3.2 and consider evolution of Mg II absorption properties with halo mass and simulation resolution in Section 3.3.

3.1. Comparing TNG50 to MEGAFLOW

In Figure 3, we show Mg II column density maps of a selection of TNG50 halos drawn from our fiducial sample at $z = 1$. The halos are aligned so that the angular momentum vector of the stars in the central galaxy points along the vertical axis; thus, the view is edge-on. The strongest Mg II columns are found within and very close to the galaxy, demarcated by a red circle with a radius of twice the galaxy's stellar half-mass–radius (the same definition used in DeFelippis et al. 2020). Beyond the galaxy, Mg II gas consistently appears to both surround the galactic disk and be very clumpy, but the amount and morphology of such gas varies greatly. In particular, there is significant variation with azimuthal angle: the highest Mg II columns generally appear in the plane of rotation, but strong columns can occur above and below the disk as well, such as in halo 265 (the bottom left panel of Figure 3). Péroux et al. (2020) found the CGM gas metallicity to vary with azimuthal angle, but interestingly, they found gas near the major axis to have lower than average metallicity in the halo, indicating that large Mg II columns do not necessarily correspond to metal-enriched gas. High Mg II columns are much less common in the outer halo ($r \gtrsim 50$ kpc), but the presence of satellite galaxies can populate that region with Mg II gas, shown most clearly in halo 340 (the bottom right panel of Figure 3).

Within our fiducial sample, it is evident that the distribution of Mg II varies drastically, presumably due to different halo formation histories. Sight lines through different halos will therefore likely produce different absorption profiles even for sight lines with identical geometries. This highlights the necessity of calculating population averages of Mg II properties from TNG50 to compare to MEGAFLOW.

We begin such a comparison with Figure 4, which shows the average strength of Mg II absorption, represented as the rest-frame equivalent width (EW_0) as a function of impact

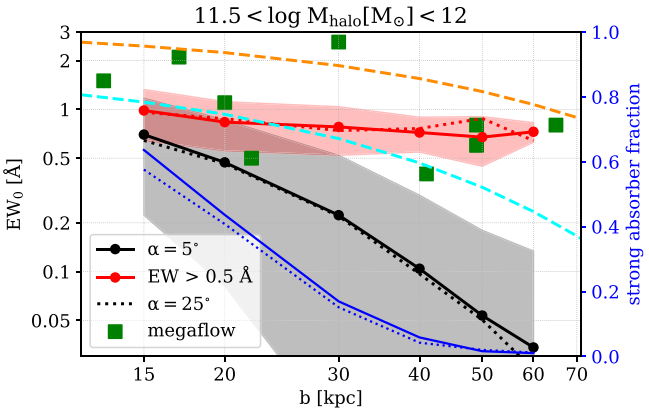

Figure 4. Mean Mg II equivalent widths of halos in our fiducial sample vs. the impact parameter of sight lines through those halos. Black and red lines and corresponding shaded regions show the mean and $\pm 1\sigma$ scatter of all halos and the subset of strong absorbers ($EW_0 > 0.5$ Å), respectively. Sight lines at a constant azimuth angle of $\alpha = 5°$ and 25° are shown with solid and dotted lines, respectively. Observations of individual accretion systems from Zabl et al. (2019) are shown as green squares. The fraction of strong absorbers as a function of impact parameter (blue) is shown with the right vertical axis. The cyan and orange dashed lines are log-linear fits of $z \sim 1$ Mg II absorbers from Nielsen et al. (2013a) and Lundgren et al. (2021), respectively.

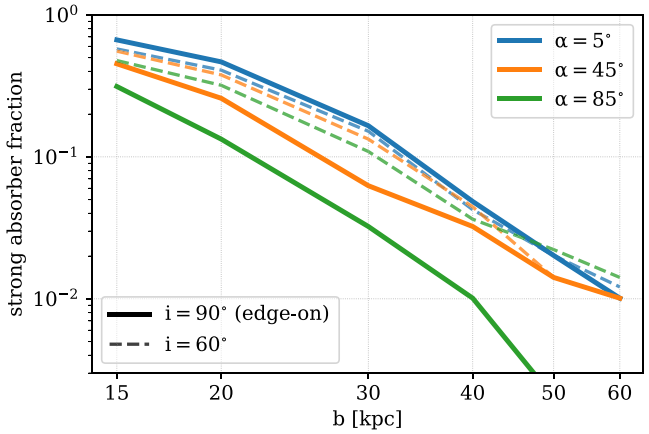

Figure 5. Mg II covering fraction of our fiducial sample as a function of impact parameter for sight lines with $\alpha = 5°$ (blue), $\alpha = 45°$ (orange), and $\alpha = 85°$ (green). Solid and dashed lines show sight lines that are edge-on and inclined at $i = 60°$, respectively.

parameter (b) for our fiducial sample. In this plot, we make an important distinction between the entire fiducial sample, shown in black, and the subset of "strong absorbers" in red. We define strong absorbers as sight lines through a halo that produce an absorption spectrum with $EW_0 > 0.5$ Å (the same as in Zabl et al. 2019). It is this "absorber-selected" subset of the fiducial sample that is most directly comparable to MEGAFLOW. For easier comparison to Figure 3, we find that sight lines with $EW_0 = 0.5$ Å have Mg II column densities ranging from $\approx 10^{13.5}$–$10^{14.5}$ cm^{-2}, i.e., just above the lower limit of the color bar.

At all impact parameters, the average rest-frame EW of the "all absorbers" sample from TNG50 (black) is smaller than those of MEGAFLOW, as expected given the selection function. The difference ranges from a factor of only ≈3 at $b \leqslant 20$ kpc to a factor of ≈30 at 60 kpc. If, instead, we compare the average EW_0 of the strong absorber subset ($EW_0 > 0.5$ Å) from TNG50, which is the appropriate comparison to make, we find the mean shown in red. This is much more similar to the values from MEGAFLOW, especially for $b \geqslant 40$ kpc, but it is still as much as a factor of ≈2 lower than the observed values at $b \leqslant 20$ kpc. However, the limited size and large scatter of the MEGAFLOW points from Zabl et al. (2019) make it difficult to assess the precise level of disagreement with TNG50. Sight lines at $\alpha = 5°$ (solid) and $\alpha = 25°$ (dotted) produce essentially identical equivalent widths over both the entire fiducial sample and the subset of strong absorbers. With the two additional dashed lines in Figure 4 we provide a point of comparison to larger samples of moderate-redshift Mg II absorbers from Nielsen et al. (2013a) and Lundgren et al. (2021). Though both of these samples have a slightly smaller equivalent-width threshold than Zabl et al. (2019) (≈0.2–0.3 Å) and no selection based on the geometry of the sight line, they still bracket both the Zabl et al. (2019) absorbers and the strong absorbers from TNG50, indicating that these simulated Mg II EWs are also consistent with observed Mg II EWs in general, given the large scatter.

The blue lines in Figure 4 show the fraction of all sight lines that host strong absorbers as a function of impact parameter. At sight lines very close to the galaxy ($b = 15$ kpc), strong absorbers are common and in fact represent a majority of all halos. However, by $b = 20$ kpc the strong absorber fraction drops below 50%, and at the largest impact parameters shown, the fraction is only ≈1%. Strong absorbers are slightly more common at $\alpha = 5°$ compared to $\alpha = 25°$, which can be understood by noting that the sight lines with smaller α pass through the disk midplane closer to the galaxy's center, where gas is generally denser. However, this difference in strong absorber fraction does not affect the measured equivalent widths, indicating that the TNG50 halos' agreement with MEGAFLOW for sight lines near the galaxies' major axes is not subject to the precise geometries of the sight lines.

In Figure 5, we examine how Mg II EWs vary throughout the entire halo in TNG50, not just near the major axis, and we find a clear trend: at all impact parameters we study, the mean EW of a perfectly edge-on sight line decreases as the azimuth angle of that sight line α increases. Sight lines near the minor axis (green) have EWs at least 0.35 dex smaller than sight lines near the major axis (blue), and sight lines between both axes (orange) have EWs between the values at both axes. This represents a disagreement between TNG50 and Mg II observations, which are generally observed to have a bimodal distribution of α near 0° and 90° (Bordoloi et al. 2011; Bouché et al. 2012; Kacprzak et al. 2012; Martin et al. 2019; Zabl et al. 2019; Lundgren et al. 2021). The distribution of α in TNG50 is clearly peaked at small α, implying that TNG50 is not producing the same kind of Mg II that is inferred to be outflowing in observations. It is also clear that this azimuthal angle dependence is very sensitive to the inclination angle of the sight line because it nearly disappears when the sight lines are inclined at an angle of 60° with respect to the axis of rotation (dotted lines in Figure 5), as would be typical for observations. This sensitivity indicates that most Mg II absorption in TNG50 comes from a gas in the vicinity of the disk midplane, where we have already seen (Figure 4) that TNG50 is consistent with observations. Therefore, for the remainder of this paper we restrict our observational comparison to sight lines near the major axis.

Having established the degree of consistency of Mg II equivalent widths, we now examine kinematic signatures of Mg II along sight lines in TNG50 and compare them to MEGAFLOW. In Figure 6, we explicitly draw the connection

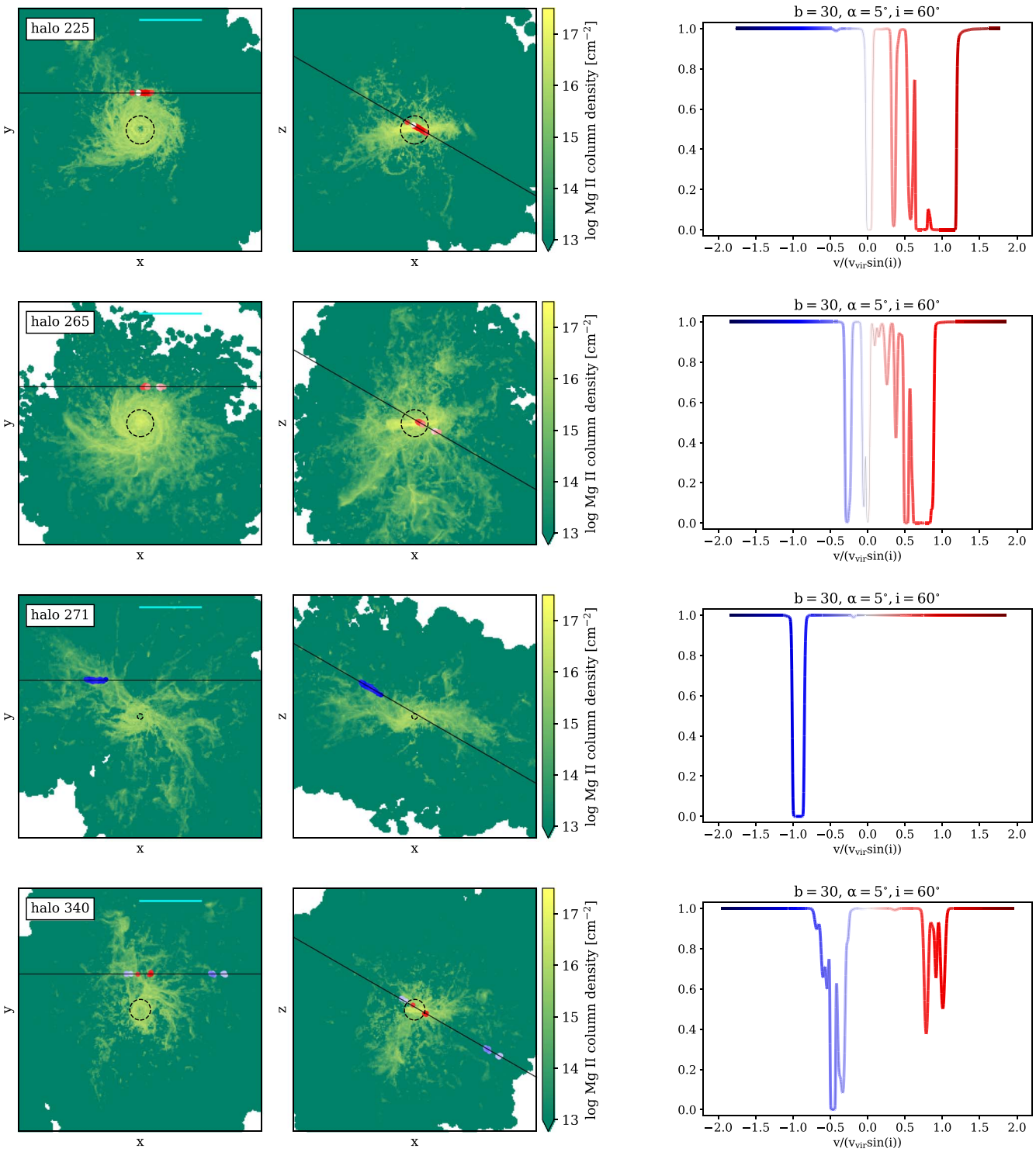

Figure 6. Each row contains two Mg II column density maps of a halo from Figure 3 projected along the vertical (left) and a horizontal (middle) axis. A sight line at $b = 30$ kpc, $\alpha = 5°$, and $i = 60°$ is overlaid along with gas cells that intersect that sight line and have a Mg II column density of at least 10^{12} cm^{-2}, which accounts for >95% of the Mg II mass along those sight lines. The Mg II gas cells and the resulting flux-normalized velocity spectrum (right) are colored by the velocity along the line of sight normalized by $V_{vir}\sin(i)$, where V_{vir} is the virial velocity of the halo. Dashed circles show twice each galaxy's stellar half-mass–radius.

between the Mg II gas cells that contribute to the column densities seen in Figure 3 and the velocity spectrum created from a subset of those cells that intersect a sight line through the halo. In each row, we show two orientations of one of the four halos from Figure 3 overlaid with a sight line with $b = 30$ kpc, $\alpha = 5°$, and $i = 60°$, and the Mg II velocity spectrum generated from that sight line. From these few examples it is clear that the gas producing the Mg II absorption is generally not distributed uniformly along any sight line: it is usually concentrated in discrete clumps in regions of the sight line nearest to the galaxy. This is seen clearly in rows one, two, and four of Figure 6, where the majority of gas cells have positive LOS velocities (i.e., corotating with the galaxy) and

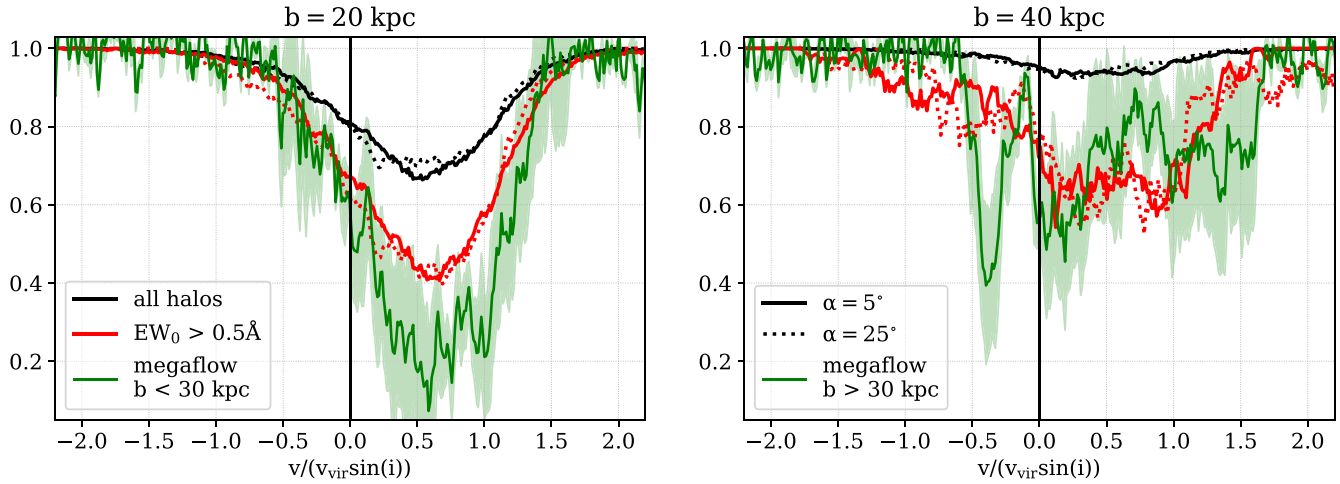

Figure 7. The stacked Mg II velocity spectra for the full fiducial TNG50 sample (black) and the subset of strong absorbers (red) for sight lines with $\alpha = 5°$ (solid) and 25° (dotted), and $b = 20$ kpc (left) and 40 kpc (right). Spectra are normalized by V_{vir} sin(i), where V_{vir} is the halo's virial velocity. The green line in each panel is the stacked spectrum of the four smallest (left) and largest (right) impact parameters from Zabl et al. (2019), and the green shaded region is an estimate of the error from bootstrapping.

produce distinct kinematic components in the spectrum that are often saturated.

It is also notable that by comparing the spectra alone it is possible to distinguish morphological differences in the Mg II distribution between halos. The first two halos, for example, have a prominent Mg II disk that both spectra reveal to be primarily corotating. The halo in row three, however, does not have such a clear disk, and the spectrum is instead composed of a cluster of counter-rotating gas cells significantly above the plane of the galaxy. The halo in row four has a spectrum with substantial corotating and counter-rotating components, which imply Mg II structure in between the ordered halos (rows one and two) and disordered ones (row three). With this small sample, we have demonstrated that the velocity spectrum, despite being composed of a very small fraction of all of the Mg II gas, is capable of reflecting the potential diversity of Mg II gas kinematics in halos of similar mass, but is also fairly consistent between halos with similar morphologies. Later in the paper, we consider whether the Mg II gas reflects the kinematics of other components of the CGM.

From these results, we now compare stacked spectra from the fiducial sample to the stacked spectra presented in Zabl et al. (2019). Figure 7 shows stacked spectra for the entire TNG50 fiducial sample (black), TNG50 strong absorbers (red), and the absorbers from Zabl et al. (2019) (green). The two panels correspond to two different impact parameters that allow a comparison between absorbers nearer to a galaxy and farther from a galaxy. In the left panel, showing stacked spectra at small impact parameters, there is a very clear kinematic picture. The strong absorber spectrum from TNG50 is symmetric, centered at $\approx 0.6 V_{vir}$, and has a FWHM of $1.2 V_{vir}$, the same as the spectrum of Zabl et al. (2019). Thus, qualitatively, strong Mg II absorbers as a population generally have LOS velocities in the same direction as their corresponding galaxies' rotations. One slight difference with the stacked spectra for strong absorbers is that the TNG50 spectrum (red) is somewhat shallower than the observed spectrum (green). However, there is essentially no difference between TNG50 spectra generated from sight lines at the two azimuthal angles $\alpha = 5°$ (solid line) and 25° (dotted line).

In Figure 7 (left), the only difference between the full fiducial spectrum and the strong absorber-only spectrum is the depth, indicating that, as a population, strong absorbers are not kinematically distinct from absorbers in general at this impact parameter. The precise reason for the discrepancy in the depth is difficult to determine, but it may be sensitive to certain parameters in the TNG physics model (e.g., metal loading of outflows from supernovae). However, it could also be an effect of simulation resolution (see Section 3.3). So, while TNG50 potentially slightly underproduces the observed amount of Mg II gas at 20 kpc, it does possess average kinematics that are consistent with observations of the same region of the CGM.

Figure 7 (right) compares the stacked spectra at a larger impact parameter ($b = 40$ kpc). The strong absorbers from TNG50 and MEGAFLOW (Zabl et al. 2019) are both shallower, wider (FWHMs of $1.3 V_{vir}$ and $2 V_{vir}$, respectively), no longer symmetric, and significantly noisier, though both are still approximately centered at a velocity on the order of $V_{vir}/2$. At this impact parameter, the depths of the simulated strong absorber and observed spectra are consistent with each other. However, strong absorbers no longer kinematically resemble the full fiducial sample: in addition to being much rarer at 40 kpc than at 20 kpc, the strong absorbers have larger positive velocities, indicating that Mg II in this region is tracing atypically faster-moving gas. As was the case at 20 kpc, the difference in the spectra between the two azimuth angles is minor. We also note here, but do not show, that the shapes and depths of individual spectra from Zabl et al. (2019) match quite well with particular individual spectra from the much larger fiducial sample from TNG50 (examples of individual spectra from TNG50 are shown in Figure 6).

3.2. 3D Kinematics of Mg II in TNG50

In this section, we characterize the three-dimensional kinematics of the Mg II gas in TNG50 and its relation to the observed quantities we discussed in Section 3.1. We show average velocity profiles of the halos in the fiducial sample in Figure 8. The top panel shows the azimuthal velocity component (v_ϕ) in spherical coordinates as a function of radius. We divide gas into cold and hot components based on a temperature threshold of 3×10^4 K, which is chosen to separate

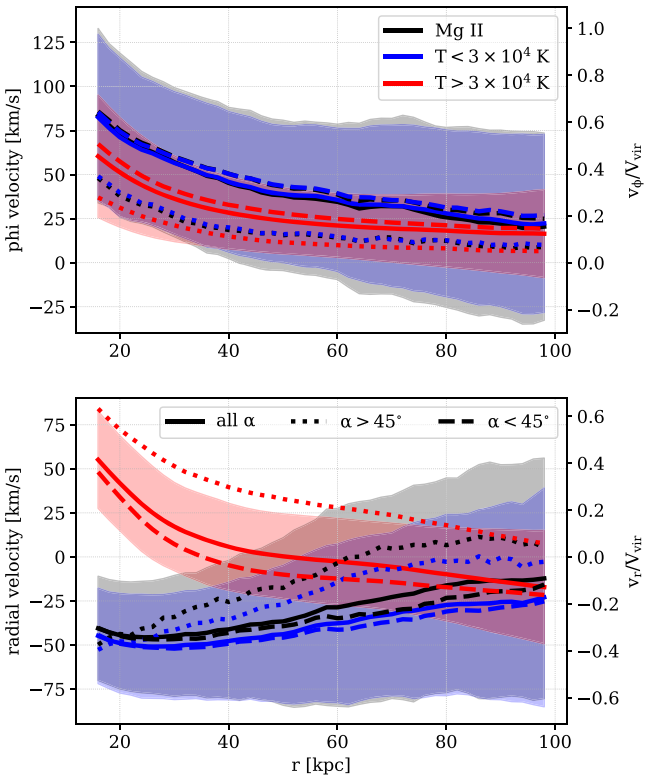

Figure 8. Mean mass-weighted velocity profiles of the spherical phi-component (v_ϕ, top) and r-component (v_r, bottom) for cold gas (blue), hot gas (red), and Mg II gas (black) in spherical bins. Velocity is given in km s^{-1} and as a fraction of the virial velocity. A temperature of 3×10^4 K is used to separate "cold" and "hot" gas. Profiles are shown for gas in the entire halo (solid), gas with $\alpha > 45°$ (dotted), and gas with $\alpha < 45°$ (dashed). Shaded regions show the $\pm 1\sigma$ scatter of the solid lines and are of similar size for all profiles.

the cold and hot clusters seen in Figure 2, although the profiles are not sensitive to the precise choice of temperature threshold. To understand the relationship of the hot and cold gas to Mg II-bearing material we also show the Mg II mass-weighted profiles.

First, we see that the Mg II gas and the cold gas have nearly identical v_ϕ profiles throughout the halo. In the innermost regions of the CGM (15–20 kpc), the cold gas has a mean azimuthal velocity of 80 km s^{-1} ($\approx 0.6 V_{\rm vir}$), while in the outermost regions (90–100 kpc), the mean azimuthal velocity decreases to 20 km s^{-1} ($\approx 0.15 V_{\rm vir}$). At all radii, the $\pm 1\sigma$ scatter is quite large ($\approx$100 km s^{-1}), though the standard errors on this and all other mean velocities in Figure 8 range from only 1–3 km s^{-1}. Though not explicitly shown, most of the cold and Mg II gas mass is closer to the major rather than the minor axis because the all-α profiles are much more similar to the $\alpha < 45°$ (dashed) profiles than the $\alpha > 45°$ (dotted) profiles. Hot gas has lower azimuthal velocities at all radii, a slightly shallower slope to its profile, and a smaller scatter in azimuthal velocity by a factor of $\approx$2 but is otherwise qualitatively similar to the cold and Mg II gas. This relationship between hot and cold gas is consistent with similar measurements of v_ϕ made from TNG100 in DeFelippis et al. (2020).

In the radial-velocity profiles (Figure 8, bottom), we see a gulf between the velocities of the hot and cold gas develop within 90 kpc. Above this radius, the average radial velocities of all components of the gas converge to -20 km s^{-1} ($\approx 0.15 V_{\rm vir}$), though the spread of radial velocities in this

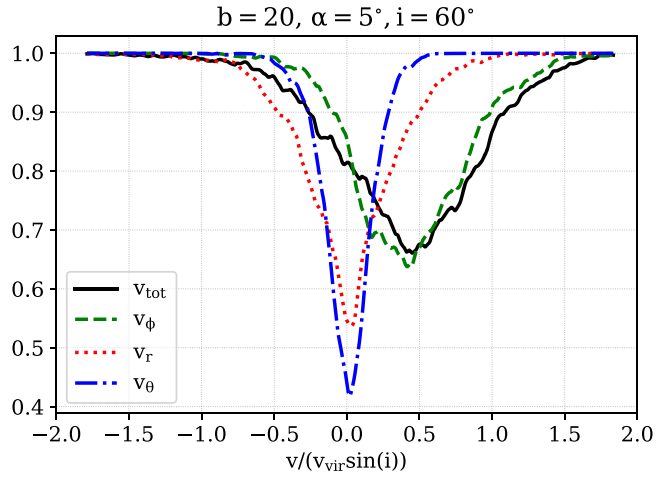

Figure 9. Stacked Mg II velocity spectra for the full fiducial TNG50 sample at a single sight line. The contributions of the three spherical components of velocity—v_r (dotted red), v_ϕ (dashed green), and v_θ (dotted–dashed blue)—are shown, as well as the spectrum created from the total velocity (solid black).

region of the CGM is very large, especially for cold gas ($\pm 1\sigma$ scatter of 120 km s^{-1}). Moving toward smaller radii, the cold gas inflow velocities become larger, while hot gas inflow velocities decrease and then switch to a net outflow at 50 kpc. The Mg II gas still traces the cold gas, which reaches typical inflowing velocities of 45–50 km s^{-1} in the inner CGM out to $r = 40$ kpc, where the spread in radial velocities is a factor of 2 smaller than in the outer halo. The geometry of accretion and outflows is evident from this panel as well: hot gas has especially large mean outflowing velocities for $\alpha > 45°$ while cold gas in the same region has a mean inflowing velocity in the inner halo and nearly no net radial motion in the outer halo. Most of the cold and Mg II gas mass is moving toward the galaxy in regions surrounding the major axis out to a substantial fraction of the virial radius. It is also clear that kinematically, Mg II gas in TNG50 is nearly identical to a simple cut on temperature and so is an excellent tracer of the kinematics of cold CGM gas. In the context of Section 3.1, these results indicate that mock Mg II spectra are representative of the entire cold phase of the CGM along the same sight lines.

Finally, we examine the 3D velocities of the Mg II gas along our sight lines. In Figure 9, we plot stacked spectra for Mg II using the three spherical velocity components individually (r, θ, and ϕ), and compare those to the spectrum generated with the full velocity of our fiducial sample of halos. Both the r and θ component spectra are centered at 0 km s^{-1}, indicating that over the entire sample they do not contribute any net velocity shift to the gas along the sight lines. The spectrum of the ϕ component is remarkably similar to the spectrum of the entire velocity, both in terms of velocity shift and width. This means that for our fiducial sample, the shape of the stacked velocity spectrum along sight lines is completely determined by only the ϕ (i.e., rotational) component of the velocity along those sight lines.

3.3. Effects of Halo Mass and Resolution on Mg II in TNG50

We now describe how our main results vary with halo mass and mass resolution. To study the effect of halo mass, we consider two mass bins containing halos from TNG50 with $10^{11}\,M_\odot < M_{\rm halo} < 10^{11.5}\,M_\odot$ and $10^{12}\,M_\odot < M_{\rm halo} < 10^{12.5}\,M_\odot$ at $z = 1$, which are above and

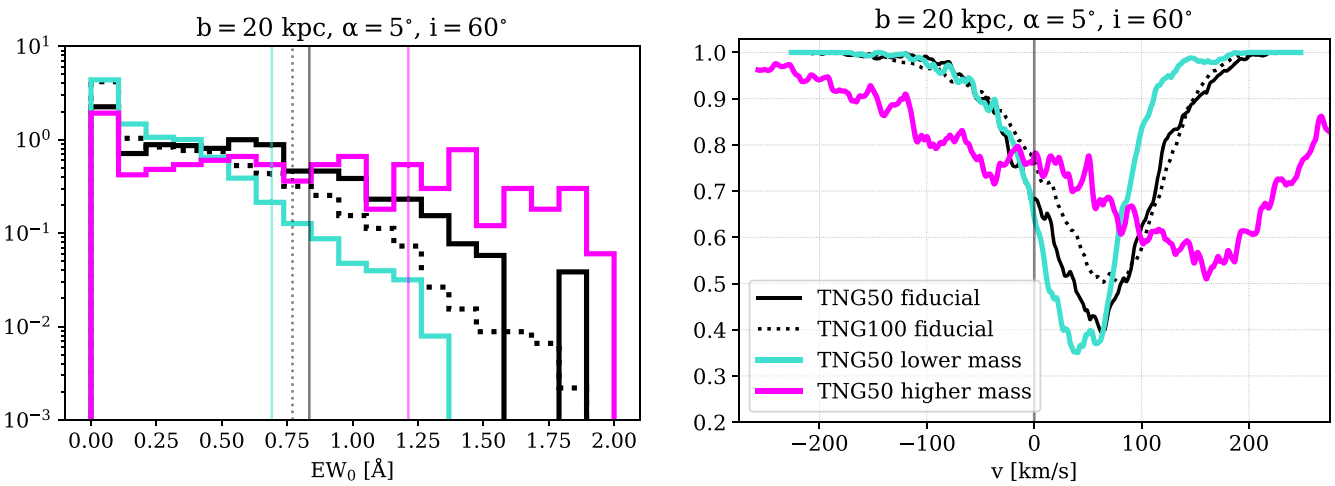

Figure 10. Left: rest-frame equivalent-width distribution of the TNG50 fiducial sample (solid black), lower-mass halos with $10^{11}\,M_\odot < M_{\rm halo} < 10^{11.5}\,M_\odot$ (cyan), higher-mass halos with $10^{12}\,M_\odot < M_{\rm halo} < 10^{12.5}\,M_\odot$ (magenta), and the same mass halos from TNG100 (dotted black) at the same sight line of $b = 20$ kpc, $\alpha = 5°$, and $i = 60°$. The mean EW$_0$ of the strong absorbers in each halo mass bin is shown with a translucent vertical line of the same color. Right: stacked velocity spectra of the same halo samples with velocities in km s^{-1}.

below the fiducial mass range and contain 1130 and 167 halos, respectively. As in Section 3.1 we calculate Mg II equivalent widths and generate velocity spectra that we show in Figure 10. For easier comparison, we also show the TNG50 fiducial sample.

As shown in the left panel of Figure 10, at a given impact parameter, the shape of the equivalent-width distribution changes with halo mass: lower halo masses (cyan) are much more likely to host weak or nonabsorbers than higher halo masses (magenta), and they are much less likely to host strong absorbers. We find this trend to hold at all impact parameters studied in this paper. We can see the effect on observability with the vertical lines in this panel, which show the mean equivalent widths of the strong absorbers in each mass bin. Typical strong absorbers in the fiducial sample have only slightly larger equivalent widths than those those at lower halo masses, but are substantially weaker than the strong absorbers at higher halo masses. At larger impact parameters, the mean equivalent widths of all strong absorbers is ≈0.8 Å, but they are exceedingly rare in lower-mass halos. Thus, the primary effects of increasing halo mass on strong absorbers are to increase their occurrence at all impact parameters, especially at large distances, and to increase the mean equivalent width of strong absorbers for halo masses $\gtrsim 10^{12}\,M_\odot$. We note that this result is qualitatively consistent with Chen et al. (2010b), who find a larger Mg II extent in the CGM of higher-mass galaxies.

Also shown in the left panel of Figure 10 is the equivalent-width distribution of 4315 halos with the same mass as the fiducial sample from the TNG100 simulation, which has a lower baryonic mass resolution than TNG50 by a factor of ∼16. Decreasing the simulation resolution lowers equivalent widths overall and steepens the distribution in the same way as decreasing the halo mass does, but the effect is weaker. The mean equivalent width of strong absorbers is largely unaffected by the change in resolution.

In the right panel of Figure 10 we examine the effect of halo mass and resolution on the observed Mg II spectrum of strong absorbers. We note that the spectra of the entire samples, as in Figure 7, have the same shape and center as their corresponding strong absorber subset, but are substantially shallower. We also plot the real velocity rather than the normalized velocity to emphasize the difference in equivalent widths, which can be more easily read off.

We see that the fiducial and lower-mass bins have remarkably similar spectra: they are both symmetric and centered at moderate positive velocities. The spectrum of the higher-mass bin is markedly different: it is much broader, asymmetric, and centered at a significantly higher velocity. It still, however, shows a preference for Mg II gas to be corotating. We note that the difference between Figure 10 as shown and the corresponding velocity-normalized spectrum (not shown) is that the normalized higher-mass spectrum is compressed slightly and therefore appears more similar to the normalized fiducial spectrum. Additionally, while the lower-mass and fiducial spectra are both centered at $\approx 0.5 V_{\rm vir}$, the higher-mass spectra are peaked at $\approx V_{\rm vir}$. Higher halo masses ($\gtrsim 10^{12}\,M_\odot$) thus have substantially more Mg II absorption and more complex kinematic signatures than for the halo masses of the fiducial sample and lower.

Finally, we consider the difference that resolution makes in the Mg II absorption spectrum. As was the case with equivalent widths, the difference caused by resolution is smaller than the difference caused by either increasing or decreasing the halo mass. Apart from a slight change in the depth of the spectrum, the kinematic properties of strong absorbers in TNG are essentially resolution independent (see solid versus dotted curves in Figure 10 for TNG50 and TNG100, respectively). The effect of increasing the resolution of the simulation is therefore primarily to increase the occurrence of strong absorbers at a given halo mass.

4. Discussion

4.1. The Role of Mg II in TNG

We consider here the ramifications of the detailed analysis of Mg II in TNG from Section 3. In Figure 8, we found that Mg II gas is very well approximated by a simple temperature cut. Therefore, we expect the angular momentum of cold gas in the CGM of TNG galaxies should be very similar to that of Mg II. DeFelippis et al. (2020) found cold CGM gas in halos of this mass range and redshift to have higher angular momentum when surrounding high-angular-momentum galaxies, meaning

Mg II is likely tracing high-angular-momentum gas in the CGM of these halos. As the velocity spectrum's center and shape is almost completely set by the rotational velocity component (see Figure 9), it should therefore be possible to use Mg II velocity spectra from sight lines near the major axis to estimate the angular momentum of cold gas in the CGM.

In Section 3.3 we examined possible halo mass and resolution dependencies of our results with two main goals in mind: to establish any broad effects of the TNG feedback model on Mg II, and to determine to what extent the cosmological simulation can capture Mg II kinematics. Feedback is known to be important for regulating gas flows into, out of, and around galaxies, and therefore could have observable signatures in the Mg II spectra, especially at different halo masses. The results of the halo mass analysis suggest that for halos with masses between $10^{11}\,M_{\odot}$ and $10^{12}\,M_{\odot}$, the physical mechanisms affecting their CGM are similar enough to result in Mg II spectra that essentially scale with the halo's virial velocity. This is presumably because feedback from supernovae is the dominant form of feedback that affects the CGM for all halo masses below $\sim 10^{12}\,M_{\odot}$ and produces Mg II gas with similar kinematic signatures. For halos above $10^{12}\,M_{\odot}$, however, Mg II gas has stronger overall absorption, as reflected by their flatter EW distribution, and substantially larger velocities and velocity dispersions, as reflected by their very broad velocity spectra. This is likely due to the dominant form of feedback switching from stars to AGN around this halo mass. However, within the higher-mass sample, halos with larger black hole masses do not themselves have broader Mg II spectra, so there is probably a combination of effects that result in a noticeable difference in the properties of the spectrum at higher masses.

Nelson et al. (2020) have recently used TNG50 to study the origin of cold Mg II gas in the CGM of very massive ($M_{*} \gtrsim 10^{11}\,M_{\odot}$) galaxies and found structures of size a few $\times 10^{2}$ pc that are sufficient to explain the observed covering fractions and LOS kinematics. They also note that while some fundamental properties like the number of cold gas clouds present in halos are not converged at TNG50's resolution, the total cold gas mass of such halos is converged in TNG50. This supports our findings that our kinematic results do not qualitatively change even going from TNG50 to TNG100, a factor of $\sim$16 in mass resolution (Figure 10), because the majority of the Mg II mass is already in the halo by TNG50's resolution. We expect higher-resolution simulations to produce more strong absorbers at a given halo mass but the rotation of Mg II near the major axis appears to be a resolution-independent aspect of the CGM for MEGAFLOW analogs in the TNG simulations.

Finally, in Figure 11, we show the specific angular momentum (j) of different halo components as a function of stellar mass of their central galaxies, with the goal of contextualizing the angular momentum of Mg II gas (black line) in the CGM in relation to the rest of the gas in the CGM as well as to the other components of the halo. The slope of this j–M_{*} relation for the stellar component of galaxies (purple line) is $\sim$0.6 as generally observed (e.g., Fall & Romanowsky 2013), and all other components appear to have roughly equal slopes. Most interesting are the relative positions of the CGM and dark matter (orange line) on this plane. At a given stellar mass, all components of the CGM have a slightly higher typical j than that of the dark matter by $\sim$0.2 dex. There are multiple

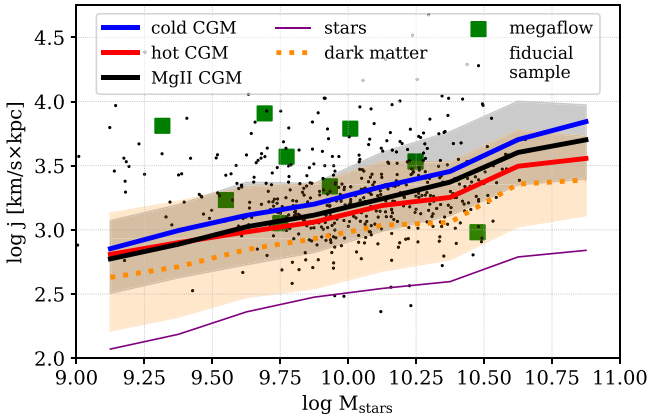

Figure 11. Median-specific angular momentum versus galactic stellar mass for the cold (blue), hot (red), and Mg II (black) CGM as defined in Figure 8, as well as the dark matter halo (dotted orange) and the stellar component of the galaxy (purple) at $z = 1$. Unlike previous figures, medians are calculated using a sample of all halos containing central galaxies with stellar masses $10^{9}\,M_{\odot} < M_{*} < 10^{11}\,M_{\odot}$. Shaded regions show the 16th and 84th percentiles of the distributions of the Mg II gas (black), which is similar in size to all components except dark matter (orange), which has noticeably larger scatter. Black points show the Mg II specific angular momentum of the halo-mass-selected fiducial sample that is biased toward higher j for $M_{*} \lesssim 10^{9.75}$. Green squares show estimations for the specific angular momentum of the major-axis absorbers using inferred rotational velocities from Zabl et al. (2019).

potential reasons for this. First, galaxies can remove low-angular-momentum gas from the CGM by accreting it and using it to form stars. Second, feedback from stars and/or AGN can also eject low-angular-momentum gas from the halo completely. Finally, dark matter in the halo can transfer some of its angular momentum to the gas. Regardless, it is clear that Mg II traces the angular momentum of the both the cold and hot components of the CGM quite well.

Also shown in Figure 11 are two sets of points representing Mg II gas in individual halos: the fiducial sample in black and the Zabl et al. (2019) sample in green, for which j was estimated using their derived rotational velocities. The two are not directly comparable since the points from Zabl et al. (2019) represent Mg II gas along a single sight line, yet they are still able to reproduce the scatter in this relation found in TNG50, though they are somewhat biased toward higher j. This bias is likely due to the selection in Zabl et al. (2019) of strong Mg II absorption near the major axis, which is where high-j cold gas tends to reside in the CGM as shown in DeFelippis et al. (2020). Nevertheless, from Figure 11 we can conclude that estimations of the angular momentum content of the CGM provided by single sight lines of Mg II can get within $\sim$0.5 dex of typical values from TNG50 over a large range of galaxy masses.

4.2. Comparisons to Recent Work

We now highlight results from previous work on Mg II absorption in observations and simulations in the context of our results. Observations of Mg II using sight lines near the major axis of galaxies have generally found that gas is corotating with the galaxy both for small impact parameters of $<$15 kpc (e.g., Bouché et al. 2016) and large impact parameters of $>$50 kpc (e.g., Martin et al. 2019). Using a lensed system, Lopez et al. (2020) observed multiple sight lines of the same CGM and measured a decreasing Mg II rotation curve that is qualitatively similar to Figure 8. However, their absorption data only go out

to ≈30 kpc. Our work suggests Mg II rotation curves should continue to decrease to at least 100 kpc, though based on the maps in Figure 3 the Mg II column densities at those distances are significantly below current observational limits.

While this paper is focused on Mg II gas near the major axis, there are also recent results suggesting Mg II outflows along the minor axis of galaxies with velocities $>100\,\mathrm{km\,s^{-1}}$ (e.g., Schroetter et al. 2019; Zabl et al. 2020). It is worth noting though that Mortensen et al. (2021) found a lensed system with Mg II on the geometric minor axis of the absorber galaxy with LOS velocities $<100\,\mathrm{km\,s^{-1}}$ and a large velocity dispersion, indicating that the kinematics of Mg II outflows may vary significantly. We showed in Figures 5 and 8 that Mg II absorption along the minor axis is weaker than along the major axis, and that there are no net Mg II outflows along the minor axis in the TNG fiducial sample. This result appears to be discrepant with the previously cited observational papers, but we defer a detailed analysis to a future paper.

Ho et al. (2020) recently studied similar aspects of Mg II absorption in the EAGLE simulation at $z \approx 0.3$ and found results broadly consistent with ours. Specifically, they measure a rotating Mg II structure around star-forming galaxies as well as a lower detection fraction of Mg II near the minor axis. They also find that higher-mass galaxies host detectable (i.e., above a fixed column density) Mg II structures out to larger distances in the CGM, which we indirectly show with the EW distributions in Figure 10, where higher-mass halos have more strong absorbers.

5. Summary

We have simulated Mg II absorption in the CGM of halos from TNG50 comparable to the major-axis sight lines observed in the MEGAFLOW survey by Zabl et al. (2019) and compared absorption and kinematic properties of the two samples. We also examined the 3D kinematics of the Mg II in TNG50. Our conclusions are as follows:

1. The equivalent widths of absorber-selected halos (i.e., strong absorbers) from TNG50 match reasonably well with the equivalent widths of major-axis sight lines from Zabl et al. (2019) (Figure 4).
2. A majority of halos are strong absorbers at the smallest impact parameter studied (15 kpc), but the strong absorber fraction drops quickly as a function of distance (Figure 4).
3. The stacked velocity spectra of TNG50 strong absorbers match the stacked spectra of Zabl et al. (2019) very well, thus supporting the physical interpretation of corotation both below 30 kpc, where the spectra are strongly peaked near $\sim 0.5 V_{\rm vir}$ and symmetric, and above 30 kpc, where the spectra are similarly peaked but are much noisier, broader, and asymmetric (Figure 7).
4. In TNG50, Mg II gas has velocity profiles nearly identical to gas below a temperature cutoff of 3×10^4 K, meaning Mg II absorption is a good proxy for cold gas kinematics in general. There is substantial rotation and typical inflow velocities of up to $50\,\mathrm{km\,s^{-1}}$ out to ∼40 kpc in the CGM (Figure 8).
5. The radial and polar velocity components by themselves do not cause any net velocity shift in the stacked spectrum, which implies that Mg II absorption kinematics alone cannot be used to measure typical inflow speeds of rotating gas in the CGM. (Figure 9).
6. Mg II absorption strengths and spectra are stronger and broader for halos more massive than the fiducial sample of $10^{11.5}$–$10^{12}\,M_\odot$ halos but do not change very much for halos less massive than the fiducial sample. Lowering the resolution from TNG50 to TNG100 only modestly changes any of the Mg II kinematic properties (Figure 10).
7. The median-specific angular momentum of the Mg II component of the CGM as a function of galactic stellar mass is very similar to that of both cold and hot CGM gas, and it is larger than that of the dark matter halo and the stars in the galaxy by ∼0.2 dex and ∼0.8 dex, respectively. Estimates of the specific angular momentum of Mg II from the Zabl et al. (2019) data are also reasonably close to the values from TNG50 to within a factor of ∼0.5 dex. (Figure 11).

This work demonstrates that generating mock Mg II observations from TNG50 generates absorption spectra that are comparable to real data. In particular, our results are consistent with the emerging picture of rotating Mg II gas found in observations and also other simulations. In future work, we plan to widen our investigation to include other ions that trace warmer and more diffuse gas, as well as follow gas at particular redshifts backward and forward through time to determine the stability of various ion structures and their role in transporting angular momentum to or from the galaxy.

We thank Johannes Zabl, Édouard Tollet, Joakim Rosdahl, and Jérémy Blaizot for insightful and useful discussions, as well as Cameron Hummels for assistance with Trident. We also thank the anonymous referee for helpful comments. D.D. acknowledges support from the Chateaubriand Fellowship of the Office for Science & Technology of the Embassy of France in the United States. N.B. acknowledges funding support from the French Agence National de la Recherche (ANR) grant "3DGasFlows" (ANR-17-CE31-0017). Flatiron Institute is supported by the Simons Foundation. G.L.B. acknowledges financial support from the NSF (grants AST-1615955, OAC-1835509) and computing support from NSF XSEDE. F.M. acknowledges support through the Program "Rita Levi Montalcini" of the Italian MUR.

Software: Trident (Hummels et al. 2017), yt (Turk et al. 2011), Cloudy (Ferland et al. 2013), NumPy (van der Walt et al. 2011), Matplotlib (Hunter 2007), and IPython (Perez & Granger 2007).

ORCID iDs

Daniel DeFelippis https://orcid.org/0000-0002-0112-7690
Nicolas F. Bouché https://orcid.org/0000-0003-0068-9920
Shy Genel https://orcid.org/0000-0002-3185-1540
Greg L. Bryan https://orcid.org/0000-0003-2630-9228
Dylan Nelson https://orcid.org/0000-0001-8421-5890
Federico Marinacci https://orcid.org/0000-0003-3816-7028
Lars Hernquist https://orcid.org/0000-0001-6950-1629

References

Bacon, R., Bauer, S., Boehm, P., et al. 2006, Proc. SPIE, 6269, 62690J
Behroozi, P. S., Conroy, C., & Wechsler, R. H. 2010, ApJ, 717, 379
Bergeron, J., & Boissé, P. 1991, A&A, 243, 344

Bergeron, J., Cristiani, S., & Shaver, P. A. 1992, A&A, 257, 417
Bordoloi, R., Lilly, S. J., Knobel, C., et al. 2011, ApJ, 743, 10
Borthakur, S., Heckman, T., Tumlinson, J., et al. 2015, ApJ, 813, 46
Borthakur, S., Heckman, T., Tumlinson, J., et al. 2016, ApJ, 833, 259
Bouché, N., Finley, H., Schroetter, I., et al. 2016, ApJ, 820, 121
Bouché, N., Hohensee, W., Vargas, R., et al. 2012, MNRAS, 426, 801
Bouché, N., Murphy, M. T., Kacprzak, G. G., et al. 2013, Sci, 341, 50
Bowen, D. V., Chelouche, D., Jenkins, E. B., et al. 2016, ApJ, 826, 50
Bryan, G. L., & Norman, M. L. 1998, ApJ, 495, 80
Burchett, J. N., Rubin, K. H. R., Prochaska, J. X., et al. 2021, ApJ, 909, 151
Burchett, J. N., Tripp, T. M., Prochaska, J. X., et al. 2019, ApJL, 877, L20
Chen, H.-W., Gauthier, J.-R., Sharon, K., et al. 2014, MNRAS, 438, 1435
Chen, H.-W., Helsby, J. E., Gauthier, J.-R., et al. 2010a, ApJ, 714, 1521
Chen, H.-W., & Tinker, J. L. 2008, ApJ, 687, 745
Chen, H.-W., Wild, V., Tinker, J. L., et al. 2010b, ApJL, 724, L176
Chen, H.-W., Zahedy, F. S., Johnson, S. D., et al. 2018, MNRAS, 479, 2547
Coil, A. L., Blanton, M. R., Burles, S. M., et al. 2011, ApJ, 741, 8
Corlies, L., Peeples, M. S., Tumlinson, J., et al. 2020, ApJ, 896, 125
Danovich, M., Dekel, A., Hahn, O., Ceverino, D., & Primack, J. 2015, MNRAS, 449, 2087
DeFelippis, D., Genel, S., Bryan, G. L., et al. 2020, ApJ, 895, 17
DeFelippis, D., Genel, S., Bryan, G. L., & Fall, S. M. 2017, ApJ, 841, 16
Diamond-Stanic, A. M., Coil, A. L., Moustakas, J., et al. 2016, ApJ, 824, 24
Dutta, R., Fumagalli, M., Fossati, M., et al. 2020, MNRAS, 499, 5022
Emerick, A., Bryan, G. L., & Mac Low, M.-M. 2019, MNRAS, 482, 1304
Fall, S. M., & Romanowsky, A. J. 2013, ApJL, 769, L26
Faucher-Giguère, C.-A., Lidz, A., Zaldarriaga, M., & Hernquist, L. 2009, ApJ, 703, 1416
Ferland, G. J., Porter, R. L., van Hoof, P. A. M., et al. 2013, RMxAA, 49, 137
Ho, S. H., Martin, C. L., Kacprzak, G. G., & Churchill, C. W. 2017, ApJ, 835, 267
Ho, S. H., Martin, C. L., & Schaye, J. 2020, ApJ, 904, 76
Ho, S. H., Martin, C. L., & Turner, M. L. 2019, ApJ, 875, 54
Huang, Y.-H., Chen, H.-W., Johnson, S. D., & Weiner, B. J. 2016, MNRAS, 455, 1713
Huang, Y.-H., Chen, H.-W., Shectman, S. A., et al. 2021, MNRAS, 502, 4743
Hummels, C. B., Smith, B. D., Hopkins, P. F., et al. 2019, ApJ, 882, 156
Hummels, C. B., Smith, B. D., & Silvia, D. W. 2017, ApJ, 847, 59
Hunter, J. D. 2007, CSE, 9, 90
Kacprzak, G. G., Churchill, C. W., & Nielsen, N. M. 2012, ApJL, 760, L7
Kacprzak, G. G., Muzahid, S., Churchill, C. W., Nielsen, N. M., & Charlton, J. C. 2015, ApJ, 815, 22
Kulkarni, V. P., Cashman, F. H., Lopez, S., et al. 2019, ApJ, 886, 83
Lan, T.-W. 2020, ApJ, 897, 97
Lan, T.-W., & Mo, H. 2018, ApJ, 866, 36
Li, F., Rahman, M., Murray, N., et al. 2021, MNRAS, 500, 1038
Liang, C. J., & Chen, H.-W. 2014, MNRAS, 445, 2061
Lopez, S., Tejos, N., Barrientos, L. F., et al. 2020, MNRAS, 491, 4442
Lopez, S., Tejos, N., Ledoux, C., et al. 2018, Natur, 554, 493
Lundgren, B. F., Creech, S., Brammer, G., et al. 2021, ApJ, 913, 50
Marinacci, F., Vogelsberger, M., Pakmor, R., et al. 2018, MNRAS, 480, 5113
Martin, C. L., Ho, S. H., Kacprzak, G. G., & Churchill, C. W. 2019, ApJ, 878, 84
Mortensen, K., Keerthi Vasan, G. C., Jones, T., et al. 2021, ApJ, 914, 92
Naiman, J. P., Pillepich, A., Springel, V., et al. 2018, MNRAS, 477, 1206
Nelson, D., Byrohl, C., Peroux, C., Rubin, K. H. R., & Burchett, J. N. 2021, MNRAS, 507, 4445
Nelson, D., Pillepich, A., Springel, V., et al. 2018, MNRAS, 475, 624
Nelson, D., Pillepich, A., Springel, V., et al. 2019, MNRAS, 490, 3234
Nelson, D., Sharma, P., Pillepich, A., et al. 2020, MNRAS, 498, 2391
Nielsen, N. M., Churchill, C. W., & Kacprzak, G. G. 2013a, ApJ, 776, 115
Nielsen, N. M., Churchill, C. W., Kacprzak, G. G., & Murphy, M. T. 2013b, ApJ, 776, 114
Nielsen, N. M., Churchill, C. W., Kacprzak, G. G., Murphy, M. T., & Evans, J. L. 2015, ApJ, 812, 83
Peeples, M. S., Corlies, L., Tumlinson, J., et al. 2019, ApJ, 873, 129
Perez, F., & Granger, B. E. 2007, CSE, 9, 21
Péroux, C., Nelson, D., van de Voort, F., et al. 2020, MNRAS, 499, 2462
Pillepich, A., Nelson, D., Hernquist, L., et al. 2018, MNRAS, 475, 648
Pillepich, A., Nelson, D., Springel, V., et al. 2019, MNRAS, 490, 3196
Putman, M. E. 2017, in Astrophysics and Space Science Library, Vol. 430, An Introduction to Gas Accretion onto Galaxies, ed. A. Fox & R. Davé (New York: Springer International), 1
Rakic, O., Schaye, J., Steidel, C. C., & Rudie, G. C. 2012, ApJ, 751, 94
Ramos Padilla, A. F., Wang, L., Ploeckinger, S., van der Tak, F. F. S., & Trager, S. C. 2021, A&A, 645, A133
Rickards Vaught, R. J., Rubin, K. H. R., Arrigoni Battaia, F., Prochaska, J. X., & Hennawi, J. F. 2019, ApJ, 879, 7
Rubin, K. H. R., Diamond-Stanic, A. M., Coil, A. L., Crighton, N. H. M., & Stewart, K. R. 2018, ApJ, 868, 142
Rubin, K. H. R., Prochaska, J. X., Ménard, B., et al. 2011, ApJ, 728, 55
Rudie, G. C., Steidel, C. C., Trainor, R. F., et al. 2012, ApJ, 750, 67
Rupke, D. S. N., Coil, A., Geach, J. E., et al. 2019, Natur, 574, 643
Schroetter, I., Bouché, N., Wendt, M., et al. 2016, ApJ, 833, 39
Schroetter, I., Bouché, N. F., Zabl, J., et al. 2019, MNRAS, 490, 4368
Schroetter, I., Bouché, N. F., Zabl, J., et al. 2021, MNRAS, 506, 1355
Springel, V. 2010, MNRAS, 401, 791
Springel, V., & Hernquist, L. 2003, MNRAS, 339, 289
Springel, V., Pakmor, R., Pillepich, A., et al. 2018, MNRAS, 475, 676
Steidel, C. C., & Sargent, W. L. W. 1992, ApJS, 80, 1
Stewart, K. R., Brooks, A. M., Bullock, J. S., et al. 2013, ApJ, 769, 74
Stewart, K. R., Kaufmann, T., Bullock, J. S., et al. 2011, ApJ, 738, 39
Stewart, K. R., Maller, A. H., Oñorbe, J., et al. 2017, ApJ, 843, 47
Suresh, J., Nelson, D., Genel, S., Rubin, K. H. R., & Hernquist, L. 2019, MNRAS, 483, 4040
Tejos, N., López, S., Ledoux, C., et al. 2021, MNRAS, 507, 663
Tumlinson, J., Peeples, M. S., & Werk, J. K. 2017, ARA&A, 55, 389
Tumlinson, J., Thom, C., Werk, J. K., et al. 2011, Sci, 334, 948
Turk, M. J., Smith, B. D., Oishi, J. S., et al. 2011, ApJS, 192, 9
Turner, M. L., Schaye, J., Steidel, C. C., Rudie, G. C., & Strom, A. L. 2014, MNRAS, 445, 794
van der Walt, S., Colbert, S. C., & Varoquaux, G. 2011, CSE, 13, 22
Vogelsberger, M., Genel, S., Springel, V., et al. 2014a, Natur, 509, 177
Vogelsberger, M., Genel, S., Springel, V., et al. 2014b, MNRAS, 444, 1518
Vogelsberger, M., Marinacci, F., Torrey, P., & Puchwein, E. 2020, NatRP, 2, 42
Weinberger, R., Springel, V., & Pakmor, R. 2020, ApJS, 248, 32
Wendt, M., Bouché, N. F., Zabl, J., Schroetter, I., & Muzahid, S. 2021, MNRAS, 502, 3733
Werk, J. K., Prochaska, J. X., Thom, C., et al. 2013, ApJS, 204, 17
Zabl, J., Bouché, N. F., Schroetter, I., et al. 2019, MNRAS, 485, 1961
Zabl, J., Bouché, N. F., Schroetter, I., et al. 2020, MNRAS, 492, 4576
Zabl, J., Bouché, N. F., Wisotzki, L., et al. 2021, MNRAS, 507, 4294
Zahedy, F. S., Chen, H.-W., Johnson, S. D., et al. 2019, MNRAS, 484, 2257
Zahedy, F. S., Chen, H.-W., Rauch, M., Wilson, M. L., & Zabludoff, A. 2016, MNRAS, 458, 2423
Zhu, G., & Ménard, B. 2013, ApJ, 770, 130